\$ SUPER

Contents lists available at ScienceDirect

#### Clinical Biomechanics

journal homepage: www.elsevier.com/locate/clinbiomech



## Finite element modelling of the sacral soft tissues under compressive loading in the context of pressure ulcer prevention: importance of the personalization of the material parameters $^{\diamond}$

Ekaterina Mukhina a,b, Pierre-Yves Rohan a,\*, Nathanael Connesson b, Yohan Payan b

- <sup>a</sup> Arts et Métiers Institute of Technology, Université Sorbonne Paris Nord, IBHGC Institut de Biomécanique Humaine Georges Charpak, HESAM Université, F-75013, Paris. France
- b Univ. Grenoble Alpes, CNRS, UMR 5525, VetAgro Sup, Grenoble INP, TIMC, 38000, Grenoble, France

#### ARTICLE INFO

# Keywords: Finite element analysis Pressure ulcer prevention Constitutive modelling Digital volume correlation Verification and validation Model evaluation Sacral region

#### ABSTRACT

*Background:* Pressure ulcers are a common occurrence in the sacrum and are frequently associated with deep tissue injury. Research has demonstrated that compression and mechanical strain contribute to tissue damage and can be employed to assess the risk of injury. Despite the existence of several finite element models based on this evidence, the experimental evaluation of localized tissue strain is rarely addressed.

*Methods:* The objective of this study is to present a proof-of-concept protocol for creating subject-specific finite element models of sacral soft tissues under compressive loading and to compare the model predictions with experimental data based on Digital Volume Correlation of MRI data. The data was collected from one asymptomatic volunteer in four loading conditions (vertical loading of 4.3 N, 6.1 N, 8 N and 11.9 N).

Findings: A comparison of DVC-derived tissue displacements with the Finite Element simulations demonstrated accurate estimations for maximum values and displacement distribution fields for all load cases, with less than 5 % discrepancy for load configurations L1-L3 and 7 % for load configuration L4. Concerning shear strains, it was observed that there were significant differences between the DVC-derived experimental tissue shear strains and the simulation predictions when generic constitutive parameters were used. The highest difference was 43 % for the highest load configuration (11.9 N).

*Interpretation:* These results demonstrate that incorporating personalized tissue properties substantially improves model fidelity, highlighting the potential of combined imaging, mechanical testing, and FE modelling for individualized risk assessment of deep tissue injury.

#### 1. Introduction

A Pressure Ulcer (PU) is defined as "a localised injury to the skin and underlying soft tissue, usually over a bony prominence, caused by sustained pressure, shear or a combination of these". It is a complication primarily related to the care and treatment of individuals who have difficulty moving or changing position including those with disabilities and the elderly. Despite increased recent attention, their incidence rate remains unacceptably high, as evidenced by the fact that 12.1 % of patients in Belgium, 8.9 % of patients in France, 11 % of patients in Germany and 10.2 % of patients in the UK suffer from pressure ulcers during their hospitalisation (Barrois et al., 2008; Lahmann et al., 2005; Vanderwee

#### et al., 2007).

Despite extensive efforts to mitigate their impact, the burden of PUs continues to grow. In the United States, while the overall prevalence has remained stable, the proportion of severe cases has increased significantly (McAuliffe et al., 2023, pp. 2008–2019), contributing to annual healthcare costs of at least \$26.8 billion (Padula and Delarmente, 2019). In Europe, prevention costs range from  $\mathfrak{f}3$ –88 per patient daily, while treatment costs can escalate to  $\mathfrak{f}470$  per patient per day (Demarré et al., 2015). These economic costs far exceed expenditures on conditions like dermatological cancers, which benefit from greater public attention and advocacy (Schreml and Berneburg, 2017).

While traditionally attributed to ischemia from sustained pressure

E-mail address: pierre-yves.rohan@ensam.eu (P.-Y. Rohan).

 $<sup>^{\</sup>star}$  This article is part of a Special issue entitled: 'Wound care technologies' published in Clinical Biomechanics.

<sup>\*</sup> Corresponding author at: Arts et Métiers Institute of Technology, Université Sorbonne Paris Nord, IBHGC - Institut de Biomécanique Humaine Georges Charpak, HESAM Université, F-75013, Paris, France.

exceeding capillary closing pressures, growing evidence indicates that shear forces and internal deformations play a critical role, especially in areas with minimal soft tissue cushioning such as the sacrum (Bouten et al., 2003; Oomens, 2013; Oomens et al., 2015). Of particular interest are the series of experiments performed at the Eindhoven University of Technology (Oomens et al., 2015) involving indentation of the tibialis anterior muscle of Brown-Norway rats. These experiments identified a damage threshold for healthy murine skeletal muscle. Skeletal muscle has been the subject of several studies (Ceelen et al., 2008; Loerakker et al., 2013; Stekelenburg et al., 2007; Traa et al., 2019). Recent work by (Traa et al., 2019) using MRI-based 3D finite element analyses in rats demonstrated that even under similar external loading, individual subjects exhibited markedly different extents of muscle damage, highlighting a subject-specific tolerance to compression-induced injury. This underscores the importance of both mechanical and biological factors in DTI development.

The sacral region is particularly vulnerable because it combines thin subcutaneous layers over a pronounced bony prominence, leading to elevated local pressures and shear stresses during bed operations. (Mimura et al., 2009) demonstrated that both surface pressures and shear forces reach their maximum at the coccygeal and lateral sacral regions during common nursing maneuvers, with slender individuals exhibiting even higher values due to reduced soft tissue thickness. Their work emphasizes that repositioning strategies (such as knee elevation or alignment with bed bending points) can partially mitigate these forces, but cannot fully eliminate the mechanical risk at these sites. This mechanical context explains why sacral PUs are frequently deep tissue injuries (DTIs), where damage originates in the muscle or fat layers beneath intact skin and progresses outward. Although the sacral site contains limited muscle compared to limb models, the fundamental mechanism of load-induced internal strain leading to cell damage remains the same. Our study specifically quantifies these strain intensities at the sacrum, addressing the anatomical differences highlighted in previous models.

The in vivo estimation of strain concentration in soft tissues is a significant challenge, particularly at the bedside. In light of this, several computational models of load-bearing soft tissue in humans have been proposed (Al-Dirini et al., 2016; Bucki et al., 2012; Levy et al., 2017; Luboz et al., 2014; Luboz et al., 2018; Macron et al., 2018; Macron et al., 2020; Rohan et al., 2023) and showed that bony prominences induce substantial stress concentrations, which explains why these areas are vulnerable to ulceration. As shown in several studies, the mechanical response is very sensitive to the input data including geometry (Moerman et al., 2017), material properties (Luboz et al., 2014) and boundary conditions.

Nevertheless, these finite element models are rarely verified (Levy et al., 2013; Sopher et al., 2010) or are verified in a way that directly reflects the internal mechanical environment of the tissues. Many studies rely on indirect comparisons, such as matching global interface pressures (Linder-Ganz et al., 2008a; Macron et al., 2018; Macron et al., 2020) which do not represent the internal spatial distribution of strains and stresses that are most relevant to tissue damage (Ceelen et al., 2008; Traa et al., 2019). This highlights the importance of experimental approaches capable of capturing these internal fields to rigorously assess and support model predictions.

Medical imaging combined with Digital Image Correlation (DIC) techniques has been shown to be promising for the quantification of localized soft tissue strains. It has been used, for example, in vitro, in tissue-mimicking phantom (Zhu et al., 2015) and, in vivo, in the human Achilles tendon (Chimenti et al., 2016) and in the quadriceps muscle (Affagard et al., 2015a, 2015b). In a recently published study (Zappalá et al., 2024), Magnetic Resonance Imaging (MRI) images combined with Digital Volume Correlation (DVC) was used for the quantification of localized soft tissue strains in buttock tissue. These novel data offer the community reference values for the comparison of predicted strain fields with experimental estimations. Other attempts have been made with

MRI to assess the deformation of the tissue during sitting. Most of these studies did not report local strains (Call et al., 2017; Sonenblum et al., 2015).

Building upon this work, the aim of this study is to present a proof-of-concept protocol for creating subject-specific finite element models of sacral soft tissues under compressive loading. We then compare the model predictions with experimental strain and displacement data obtained using Digital Volume Correlation (DVC) of MRI scans collected on one asymptomatic volunteer under four controlled loading conditions (vertical loads of 4.3 N, 6.1 N, 8 N, and 11.9 N).

#### 2. Materials and methods

#### 2.1. Participant

One healthy male volunteer (34 y.o., 1.75 m and BMI 27.8 kg/m<sup>2</sup>) was enrolled after informed consent and local ethics committee agreement (MAP-VS protocol N°ID RCB 2012-A00340–43).

#### 2.2. MRI data acquisition

All MRI scans were performed on a 3 T Achieva dStream system (Philips Healthcare) at the IRMaGe platform, Université Grenoble Alpes. A proton density-weighted 3D acquisition was used. No inversion recovery was applied. Two surface body coils were placed on either side of the pelvis in the medio-lateral direction to enhance signal-to-noise ratio (Fig. 1(c)). The acquisition produced 512 consecutive slices (0.3125 mm thickness), yielding 3D volumes with 800  $\times$  800  $\times$  240 voxels and an isotropic resolution of 0.5  $\times$  0.5  $\times$  0.5 mm. Each scan required approximately 10 min. Respiratory gating was employed to reduce motion artefacts. To change the load between acquisitions, a brief pause of about 5 min was included, during which the participant was instructed to maintain the same position.

Controlled vertical compressive loads (0–1.2 kg) were applied to the sacrum using the custom MR-compatible setup described in (Mukhina et al., 2022). This device employed a 3D-printed indenter (118  $\times$  28  $\times$  14 mm³, 410 mm² contact area) replicating a SL10–2 ultrasound probe (Fig. 1(a)). Loads were applied in four steps (~400 g or 200 g increments), resulting in load cases L1–L4 with mean forces of 11.9 N, 8 N, 6.1 N, and 4.3 N, respectively (SD  $\leq$  2 g  $\approx$  0.02 N). Assuming a contact area of 410 mm², these correspond to pressures of approximately 29.0 kPa, 19.5 kPa, 14.9 kPa, and 10.5 kPa.

The setup ensured perpendicular loading without shear via a rigid tube structure and dead weights. To check if the US plane remained vertical during the experiment, a cylindrical reflective marker (Fig. 1(b)) was glued on the side of the indenter oriented toward the head of the participant. MRI scans were acquired under each loading condition with the participant prone on a flat surface (Fig. 1(c)), a soft support under the thorax to keep the sacral region horizontal, and respiratory gating to minimize artefacts.

For illustration, Fig. 1(d) shows a transverse (axial) slice at the level of the sacrum (around S2) from the unloaded case (L0), and Fig. 1(e) from the highest load case (L1).

#### 2.3. Personalized geometrical model

The 3D model geometry was designed using the MR 3D image recorded in the undeformed configuration L0. Fat, fascia, muscles, and bone tissues were manually segmented using Amira 2019.1 software (FEI Visualization Sciences Group, Mérignac Cedex, France). The region of interest (ROI) for 3D modelling in relation to the full MR image is shown in Fig. 2(a). Fig. 2 (b) shows the segmented volumes containing two layers of adipose tissue, separated by a fascia which has also been modeled, and muscles.

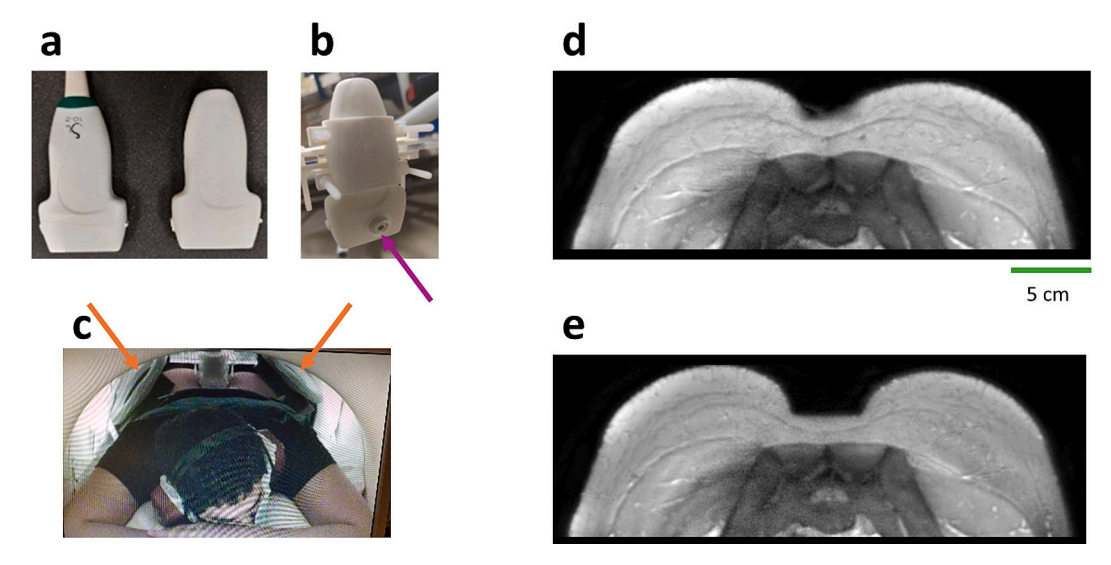


Fig. 1. (a) Real US probe (left) and associated 3D-printed copy (right); (b) Arrow showing the cylindrical reflective marker attached to the 3D-printed indenter. (c) Participant lying in the MR scanner with two surface body coils (arrows) placed on either side of the pelvis; (d) transverse MR image corresponding to the Unloaded case (L0). (e) transverse MR image of the loaded case (L1).

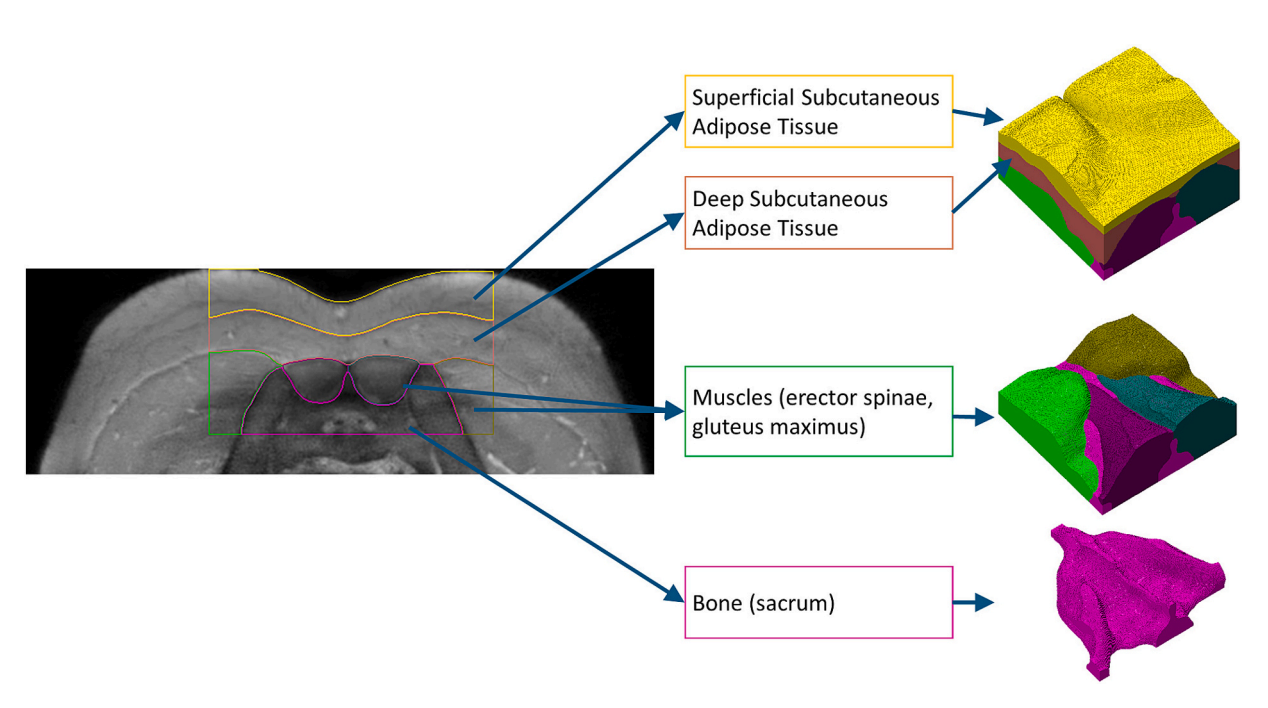


Fig. 2. (a) Transverse (axial) MR cross-sectional view at the sacral level showing anatomical structures segmented for the model: superficial and deep subcutaneous adipose tissues, erector spinae muscles, gluteus maximus muscles, and underlying bones. (b) 3D personalized finite element model reconstructed from the MRI data, with distinct colors representing adipose tissue, muscle layers, and bone.

#### 2.4. Constitutive modelling and calibration

A Yeoh hyperelastic constitutive model, previously proposed in literature (Fougeron et al., 2022), was used to model the mechanical behaviour of skin, adipose tissue, fascia and muscle. This model assumes a strain-energy function W given by the following analytical expression (1):

$$W = C_{10}(\overline{I_1} - 3) + C_{20}(\overline{I_1} - 3)^2 + C_{30}(\overline{I_1} - 3)^3 + \frac{1}{d_1}(J - 1)^2 + \frac{1}{d_2}(J - 1)^4 + \frac{1}{d_3}(J - 1)^6$$
(1)

where  $\overline{I_1}$  is the first invariant of the left Cauchy-Green deformation

tensor,  $C_i$  are material parameters, J is the determinant of the deformation gradient  $\underline{F}$ , and  $d_i$  are material parameters related to compressibility. These  $d_i$  parameters were assumed to be equal and related to the Poisson ratio  $\nu$  (Mott et al., 2008) (2):

$$d_1 = d_2 = d_3 = \frac{3^*(1-2^*\nu)}{2{C_{10}}^*(1+\nu)} \tag{2} \label{eq:d1}$$

To represent the nearly-incompressible behaviour of soft tissues, a Poisson ratio of 0.49 was assumed, similarly to ratios commonly proposed in previous models (Levy et al., 2017; Linder-Ganz et al., 2009; Luboz et al., 2018).

As a first approximation, generic values for the  $C_i$  material parameters representing skin, adipose tissue, fascia and muscle were computed

using an optimized curve fitting procedure based on tension and compression experimental tests published in the literature for these tissues (Astruc et al., 2018; Gras et al., 2012; Miller-Young et al., 2002; Ní Annaidh et al., 2012). In a second step, a personalization of the  $C_{10}$  material parameters of skin and adipose tissues based on VLASTIC suction data (Briot et al., 2022; Connesson et al., 2023; Mukhina et al., 2022) was proposed.

Briefly, our group recently introduced a lightweight, disposable aspiration system, reduced to a simple tube with a customizable head aperture (in size, shape, and material), designed to withstand stringent sterilization processes (Connesson et al., 2023; Elahi et al., 2018; Elahi et al., 2019). This method, termed VLASTIC, measures the in vivo stiffness of soft tissues by applying low-intensity suction (<40 mbar) and recording pressure-volume curves. Young's moduli are then estimated via inverse analysis using a finite element model of the suction experiment. This approach assumes (i) small strain levels appropriate for linear approximations, (ii) isotropic material behaviour in the probed regime, (iii) a bilayer structure with a perfectly bonded interface between skin and adipose tissue, and (iv) negligible contributions from deeper layers such as muscle, which are not substantially deformed under these low suction pressures. The device was first validated on homogeneous silicone phantoms, showing errors below 7 % compared to classical tensile tests (Elahi et al., 2019) and subsequently applied in vivo in a clinical pilot study to assess tongue stiffness, (Kappert et al., 2021). More recently, VLASTIC was extended to characterize bilayer materials, with tests on bilayer silicone phantoms demonstrating layerspecific stiffness estimates with errors below 10 % (Connesson et al., 2023) and subsequently in vivo to estimate the skin and fibroglandular breast tissue stiffness of seven healthy volunteers, treating the breast as a bilayer structure probed in three regions (Briot et al., 2022).

### 2.4.1. Generic material parameters estimated from data reported in the literature

#### a) Skin

Annaidh and colleagues provided data from uniaxial tensile tests performed on skin samples harvested from the region of the sacrum (Annaidh et al., 2012). The corresponding stretch/stress curve (Fig. 3(a), blue circle points) was used to fit the Yeoh constitutive parameters (Fig. 3(a), blue line; (Fougeron et al., 2022)). A fitting was obtained with two coefficients only, namely  $C_{10}=0.3$  MPa and  $C_{20}=1.9$  MPa.

#### b) Adipose tissue.

Miller-Young and colleagues provided data from unconfined compression tests performed on adipose tissue samples harvested from the heel fat pad (Miller-Young et al., 2002). The corresponding stretch/

stress curve (Fig. 3(b) blue circle points) was used to fit the Yeoh constitutive parameters (Fig. 3(b), blue line). As with the skin, a good fitting was obtained with two coefficients only, namely  $C_{10}=0.7~\mathrm{kPa}$  and  $C_{20}=0.3~\mathrm{kPa}$ .

#### c) Muscle.

Gras and colleagues performed uniaxial tensile tests on a harvested sternocleidomastoideus muscle (Gras et al., 2012). The corresponding stretch/stress curve (Fig. 3(c), blue circle points) was used to fit the Yeoh constitutive parameters (Fig. 3(c) blue line). In that case, three coefficients were required to fit the curve, namely  $C_{10}=5\text{e-}3$  MPa,  $C_{20}=6.9\text{e-}2$  MPa and  $C_{30}=1.97$  MPa.

#### d) Fascia.

Fascia constitutive parameters ( $C_{10}=0.1$  MPa,  $C_{20}=0.18$  MPa) were assumed from the experimental data that was collected and fitted by Astruc and colleagues (Astruc et al., 2018), from uniaxial tensile tests performed on a longitudinal sample harvested from posterior rectus sheath in the abdominal wall.

# 2.4.2. Personalization of the material parameters based on VLASTIC data To the best of our knowledge, there is no valid methodology for the in vivo characterization of the non-linear hyperelastic behaviour of human soft tissues. However, the VLASTIC device can be used to estimate the linear part of the stretch/stress curves, at small strains levels. Moreover, as proposed in Connesson et al. (Connesson et al., 2023), both

mate the linear part of the stretch/stress curves, at small strains levels. Moreover, as proposed in Connesson et al. (Connesson et al., 2023), both skin and fat stiffness can be estimated from local suction if a bi-layer structure is assumed for skin and adipose tissue. Equivalent Young moduli of both layers are therefore estimated based on repeating low intensity suction tests using cups of various diameters.

Based on the data collected with the VLASTIC device on the healthy volunteer included in this study (Mukhina et al., 2022), the average Young modulus was 37.7 kPa for the skin and 1.8 kPa for the adipose tissue. Assuming quasi-incompressibility, a direct relationship can be provided between the equivalent Young modulus and the material parameter  $C_{10}$  (3):

$$c_{10} \approx \frac{E}{6} \tag{3}$$

The generic  $C_{10}$  constitutive parameters of skin and adipose tissue as estimated above from the curve fitting process were therefore changed to the values provided by the in vivo suction measure, namely  $C_{10\mathrm{Skin}} = 37.7/6 = 6.3$  kPa and  $C_{10\mathrm{Fat}} = 1.8/6 = 0.3$  kPa. The corresponding changes have a visible consequence on the stretch/stress curve for skin an adipose tissue. The subject-specific new curves are drawn in red in Fig. 3(a) and Fig. 3(b), respectively.

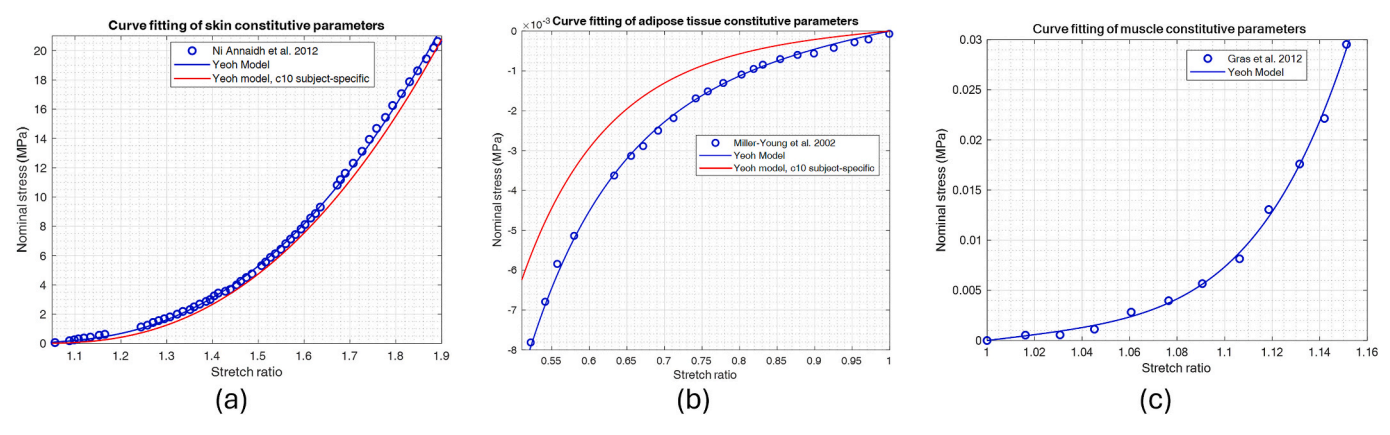


Fig. 3. (a) Skin stretch/stress experimental data after uniaxial tension (blue circles) fitted by a Yeoh constitutive model (blue curve). The red curve corresponds to the subject-specific update of the  $C_{10}$  parameter after VLASTIC suction measurements ( $C_{10} = 6.3$  kPa). The blue line represents 'literature-based' data. (b) Adipose tissue stretch/stress experimental data after compression (blue circles) fitted by a Yeoh constitutive model (blue curve). The red curve corresponds to the subject-specific update of the  $C_{10}$  parameter after VLASTIC suction measurements ( $C_{10} = 0.3$  kPa). (c) Curve fitting of muscle constitutive parameters presenting experimental data (blue circles) and fitted Yeoh model (blue curve). (For interpretation of the references to colour in this figure legend, the reader is referred to the web version of this article.)

**Table 1**Soft tissues material parameters implemented in the personalized FE model.

	c <sub>10</sub> , [MPa]	c <sub>20</sub> , [MPa]	c <sub>30</sub> , [MPa]	d <sub>1</sub> , [MPa <sup>-1</sup> ]	$egin{aligned} & d_2, & \\ & [MPa^{-1}] & \end{aligned}$	d <sub>3</sub> , [MPa <sup>-1</sup> ]
Skin	6.3e-3	1.9	-	3.2	3.2	_
Adipose tissue	0.3e-3	0.3e-3	-	66.16	66.16	_
Fascia	0.1	0.18	-	0.2	0.2	_
Muscle	5e-3	6.9e-2	1.97	4.03	4.03	4.03

Table 1 synthetizes all the values for the constitutive parameters finally implemented in our subject-specific numerical model. Skin, adipose tissue and fascia are represented by 2nd order Yeoh model, therefore, four parameters are listed. Muscle tissue is represented by 3rd order Yeoh model, therefore, six parameters are shown in Table 1.

#### 2.4.3. Material parameters of the indenter

To simulate the indentation forces exerted on the sacrum, the indenter was modeled with a linear elastic model assuming a Young modulus of 200 GPa and a Poisson ratio of 0.3.

#### 2.5. External mechanical loading

A vertical load of 11.9 N, 8 N, 6.1 N and 4.3 N was imposed by the indenter by adding dead-weights to the experimental setup corresponding to load levels L1 to L4 (Mukhina et al., 2022).

#### 2.6. FE discretization and contact modelling

The FE mesh of the sacral soft tissues was created with Hypermesh software, from the 3D surfaces extracted after the segmentation of the MR volume and imported into ANSYS Mechanical APDL. Skin and fasciae were represented as shell elements based on the surfaces delimiting the segmented tissues. Two layers of fascia were modeled: the superficial fascia separating the two layers of adipose tissues and the deep fascia located between adipose tissue and muscle. Linear tetrahedral SOLID185 elements were used for adipose tissue and muscles, while skin and fasciae were approximated by shell elements SHELL181 with thickness of 2.9 mm and 0.5 mm respectively. Bending was restricted for the shell elements leaving only the membrane properties for element stiffness.

The surface of the sacral bone in contact with muscles and adipose tissues was fixed for all DOFs. Contact nodes between two types of soft tissues were merged to avoid any complex sliding contacts between two tissue layers. A contact pair with frictionless standard behaviour of the contact surface was defined between the indenter and the skin.

One node on the top of the indenter was chosen as a pilot node (Fig. 4) for load application. A quasi-static analysis was run with two load steps, with displacement, then load, being applied to the pilot node: 1st - displacement until the contact, 2nd - load of 11.9 N for the model of Load case 1 (L1); 8 N for the model of Load case 2 (L2); 6.1 N for the model of Load case 3 (L3) and 4.3 N for the model of Load case 4 (L4).

#### 2.7. Mesh sensitivity

A mesh convergence analysis was performed by testing five different mesh sizes (element size 6 mm to 1.5 mm), resulting in maximal vertical displacements (under a 11.9 N load) ranging from 14.2 mm for the coarsest mesh (element size 6 mm) to 17.4 mm for the finest mesh (element size 1.5 mm). The relative difference between the two finest meshes (3 mm and 1.5 mm) was approximately 7 %, despite the total number of soft tissue elements increasing by more than sixfold (from  $\sim\!315,\!000$  to  $\sim\!2.3$  million). Based on this quantitative assessment, the mesh with 3 mm elements was selected as it provided a satisfactory trade-off between computational efficiency and result stability.

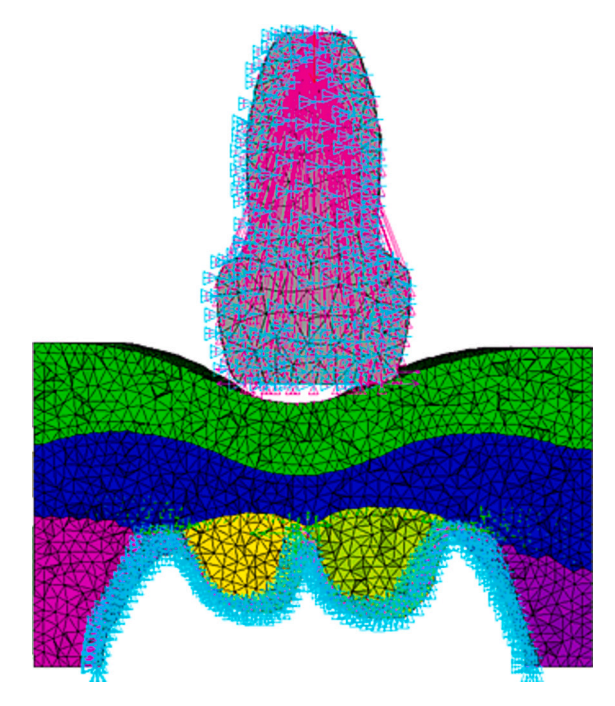


**Fig. 4.** Boundary conditions shown on a transverse cut through the FE model. Restricted displacements are represented as blue triangles, while the coupling of the indenter nodes to a pilot node is represented as pink triangles. (For interpretation of the references to colour in this figure legend, the reader is referred to the web version of this article.)

#### 2.8. ANSYS simulation post-processing

The vertical displacement of soft tissues and the maximum shear strain (4) which was previously associated with tissue damage (Ceelen et al., 2008) were extracted.

$$\epsilon_{\textit{shear}} = \frac{1}{2} max(|\epsilon_1 - \epsilon_2|, |\epsilon_2 - \epsilon_3|, |\epsilon_3 - \epsilon_1|) \tag{4} \label{eq:epsilon}$$

where  $\epsilon_1,\,\epsilon_2$  and  $\epsilon_3$  are the principal strains.

In ANSYS, EPEL, which denotes elastic strain intensity, is equivalent to maximal shear strain and is determined as the highest of the absolute values  $\epsilon_1$ - $\epsilon_2$ ,  $\epsilon_2$ - $\epsilon_3$ ,  $\epsilon_3$ - $\epsilon_1$ , where  $\epsilon_1$ ,  $\epsilon_2$  and  $\epsilon_3$  are the principal Hencky (logarithmic) strains (5). This results in a value twice larger than the classic definition of the maximum shear strain.

$$\varepsilon_{\textit{shear\_ansys}} = \max(|\varepsilon_1 - \varepsilon_2|, |\varepsilon_2 - \varepsilon_3|, |\varepsilon_3 - \varepsilon_1|) \tag{5}$$

For the rest of the paper, the ANSYS definition of maximum shear strain will be used for the presentation of all values and results.

#### 2.9. Plane of interest

A plane of interest was first defined by manually selecting anatomical points on the MR images to align with the mid-plane of the US probe piezoelectric transducer surface. Specifically, two points (A and B) were selected on the sagittal slice along the posterior edge of the transducer to determine its midpoint (Fig. 5b), while four points (C, D, E, F) were chosen on the frontal slice at the superior and inferior boundaries of the indentation mark to define the mid-edge (Fig. 5b). This construction ensured that the resulting vertical transverse (axial) plane passed through the center of the indentation region, capturing the zone of maximum deformation. This plane intersects the sacral region approximately between the first (S1) and second (S2) sacral vertebrae. All subsequent results were plotted on this plane, focusing on the deformed shape of the soft tissues within the selected region of interest (ROI).

Fig. 5. (a) Sagittal view of the 3D printed indenter; (b) Sagittal MR slice showing the points A and B manually selected to determine the midpoint on the transducer surface in the sagittal plane. (c) Frontal MR slice showing the points C, D, E, and F manually selected to define the mid-plane in the frontal plane. The positions of L5, S1, and S2 are indicated.

#### 2.10. Image registration procedure

To quantify internal displacements between unloaded and loaded configurations, a 3D image registration procedure was implemented using the Elastix library (Klein et al., 2010). The registration sought to compute a non-rigid deformation field u(x) describing how the reference unloaded image transforms into the loaded image, such that applying this deformation yields a transformed image  $I_0(x+u(x))$  that closely matches the deformed configuration.

The optimization was performed by minimizing a cost function measuring image similarity, based on the Advanced Normalized Correlation Coefficient (ANCC), consistent with approaches described by (Machado et al., 2019). To enhance convergence and avoid local minima, an adaptive stochastic gradient descent algorithm was applied within a hierarchical four-level multi-resolution framework. Intensity interpolation at non-grid points was performed using cubic B-splines, ensuring smooth deformation fields.

The registration was performed between the *fixed* MRI volume (undeformed configuration, i.e. load case L0) and each *moving* MRI volume (loaded configurations, i.e. load cases L1-L4). Voxels of the fixed image were spatially mapped to the voxels of the moving image using a 2-step procedure. First, a rigid body transformation was defined by assuming that the MRI volume is a rigid body. The parameters of the transformation were computed as those that minimized the distance between the bones in the fixed image and the bones in each moving image based on a manually defined mask (image segmentation), assuming the bony region as non-deformable. Second, B-spline non-rigid transformations were calculated between the aligned moving image and the fixed image. The coefficients of the B-spline transformations were optimized in each cube of a 3D grid that sampled the MR volume (size of the grid: 12 mm).

#### 2.11. DVC verification

The uncertainty and accuracy of the DVC pipeline used here were extensively evaluated in our previous study (Trebbi et al., 2022). This included multiple registrations of repeated unloaded acquisitions to assess reproducibility (zero-strain noise analysis) and synthetic tests with known displacement fields derived from FE models to quantify accuracy. Bland–Altman analyses confirmed low errors across the range of measured strains. Given that the same pipeline and parameter settings were used in this study, we refer the reader to (Trebbi et al., 2022) for full methodological details and error quantification.

#### 2.12. From displacement to strain field

Displacement fields were extracted from both DVC and results of ANSYS simulations for each load case. Shear strain field was derived from displacement field based on following formulas:

The right Cauchy-Green deformation tensor (6) was derived from the

deformation gradient F:

$$\underline{\mathbf{C}} = \underline{\mathbf{F}}^T \underline{\mathbf{F}} \tag{6}$$

Then, the principal Logarithmic Hencky strain was calculated as (7):

$$\varepsilon_{principal} = \frac{1}{2} \ln \underline{C} \tag{7}$$

The maximum shear strain according to the ANSYS terms (double of the classical definition of the maximum shear strain according to Hencky) has been derived in the following way (8):

$$\varepsilon_{\textit{shear}} = \max(|\varepsilon_1 - \varepsilon_2|, |\varepsilon_2 - \varepsilon_3|, |\varepsilon_3 - \varepsilon_1|) \tag{8}$$

#### 3. Results

The results focus on two sets of comparisons: (1) between experimental measurements from DVC and finite element (FE) simulations with personalized material properties, across four loading conditions (L1-L4 corresponding to  $\sim 11.9$  N, 8 N, 6.1 N, 4.3 N) and (2) between the generic and personalized FE models themselves, to assess how personalization of skin and adipose material parameters improved agreement with DVC measurements. Table 2 summarizes the maximum vertical displacements (Dz) and Hencky shear strains across all load cases. It shows how personalization of material properties substantially reduced discrepancies with respect to the DVC measurements. For vertical displacements, personalization decreased errors from 33 to 38 % (generic model) down to 2–7 % across the four loading conditions. Similarly, for shear strains, discrepancies decreased from 57 to 63 % with generic

Table 2: Summary of maximum vertical displacements (Dz) and Hencky shear strains across four loading conditions (L1–L4), comparing digital volume correlation (DVC) measurements with finite element (FE) simulations using generic and personalized material properties. Discrepancies are reported as percentages relative to DVC measurements, demonstrating the improvement in agreement achieved through material parameter personalization.

	L1 (~11.9 N)	L2 (~8 N)	L3 (~6.1 N)	L4 (~4.3 N)
Max Dz (DVC) [mm]	17	13.2	12.2	10
Max Dz (FE generic)	11.4	9	8	6.2
Max Dz (FE personalized)	16.2	13.8	12.4	10.7
ΔDz vs DVC (%) generic	33 %	32 %	34 %	38 %
ΔDz vs DVC (%) personalized	5 %	5 %	2 %	7 %
Max shear (DVC)	2.1	1.4	1.4	1.1
Max shear (FE generic)	0.9	0.6	0.6	0.4
Max shear (FE personalized)	1.2	1.0	0.9	0.8
ΔShear vs DVC (%) generic	57 %	57 %	57 %	63 %
ΔShear vs DVC (%) personalized	20 %	29 %	28 %	34 %

properties to 20–34 % after personalization.

## 3.1. Comparisons between experimental measurements from DVC and FE simulations with personalized material properties, across four loading conditions

Fig. 6 presents the comparisons between ANSYS simulations and DVC measurements for each load case. Table 2 summarizes the maximum vertical displacements and shear strains derived from DVC and FE simulations across all loading conditions, alongside their relative differences. Displacement distributions exhibited similar spatial patterns across methods, which supports the plausibility of the FE modelling approach. The highest vertical displacement predicted by the FE model was 16.2 mm for L1, closely matching the DVC measurement of 17 mm. Displacements decreased to 13.8 mm for L2 (vs. 13.2 mm DVC), 12.4 mm for L3 (vs. 12.2 mm DVC), and 10.7 mm for L4 (vs. 10 mm DVC). For Hencky shear strains, both DVC and FE simulations showed comparable distributions, with maxima located within the adipose tissue directly beneath the indentation mark. However, the FE model consistently underestimated peak shear strains. Under L1, maximum shear strain reached 1.2 in the FE simulation compared to 2.1 from DVC; for L2, 1.0 vs. 1.4; for L3, 0.9 vs. 1.4; and for L4, 0.8 vs. 1.1.

To complement the qualitative maps, Fig. 7 provides histograms comparing the distributions of axial displacements (Dz), in-plane shear strains ( $|\varepsilon_{xy}|$ ) and out-of-plane shear strains ( $\sqrt{\varepsilon_{xz}^2 + \varepsilon_{yz}^2}$ ) between the DVC measurements and the FE simulations for the highest load case (1.2 kg). These distributions confirm the overall agreement between approaches while highlighting the tendency of the FE model to slightly underestimate the shear strain magnitudes, especially for the out-of-

plane components. As the loading-dependent patterns were consistent across cases, only the highest load is shown here.

### 3.2. Effect of personnalisation on FE model agreement with DVC measurements

The simulation results for load cases L1 - L4 for two FE models compared with the DVC results are presented in Fig. 8. The first model is defined with generic material properties for all soft tissues The second model is updated with the personalized material properties for skin and adipose tissues. The discrepancy between the DVC and ANSYS simulation results reduced for the models with personalized vs generic material properties for the displacement and the Hencky shear strain values respectively by 31 % and 20 % for L1, 29 % and 29 % for L2, 36 % and 28 % for L3 and 29 % and 34 % for L4.

#### 4. Discussion

The aim of this study was to present a proof-of-concept protocol for creating subject-specific finite element (FE) models of sacral soft tissues under compressive loading, and to compare the model predictions with experimental data derived from Digital Volume Correlation (DVC) of MRI acquisitions in a healthy volunteer under four different load conditions. While earlier studies by (Al-Dirini et al., 2016; Macron et al., 2018; Segain et al., 2025) explored personalized FE modelling of the buttock region, typically combining geometry personalization with some degree of boundary condition or material adjustment, this is to our knowledge the first work to extend such an approach specifically to the sacral area. This represents a meaningful advance given the anatomical

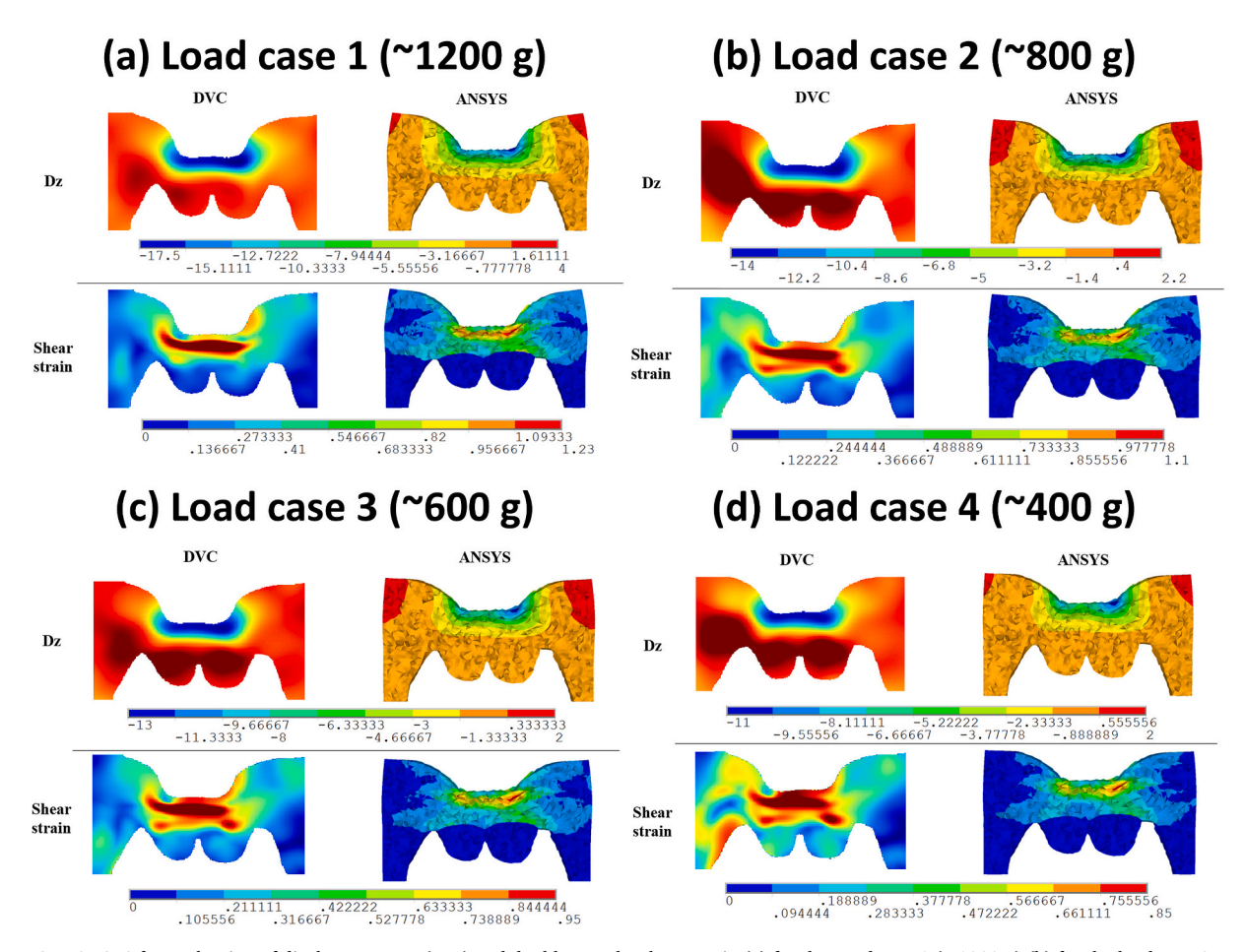


Fig. 6. DVC vs ANSYS for evaluation of displacement Dz (mm) and double Hencky shear strain (a) for the Load case 1 (~1200 g) (b) for the load case 2 Load case 2 (~800 g) (c) Load case 3 (~600 g) (d) Load case 4 (~400 g).

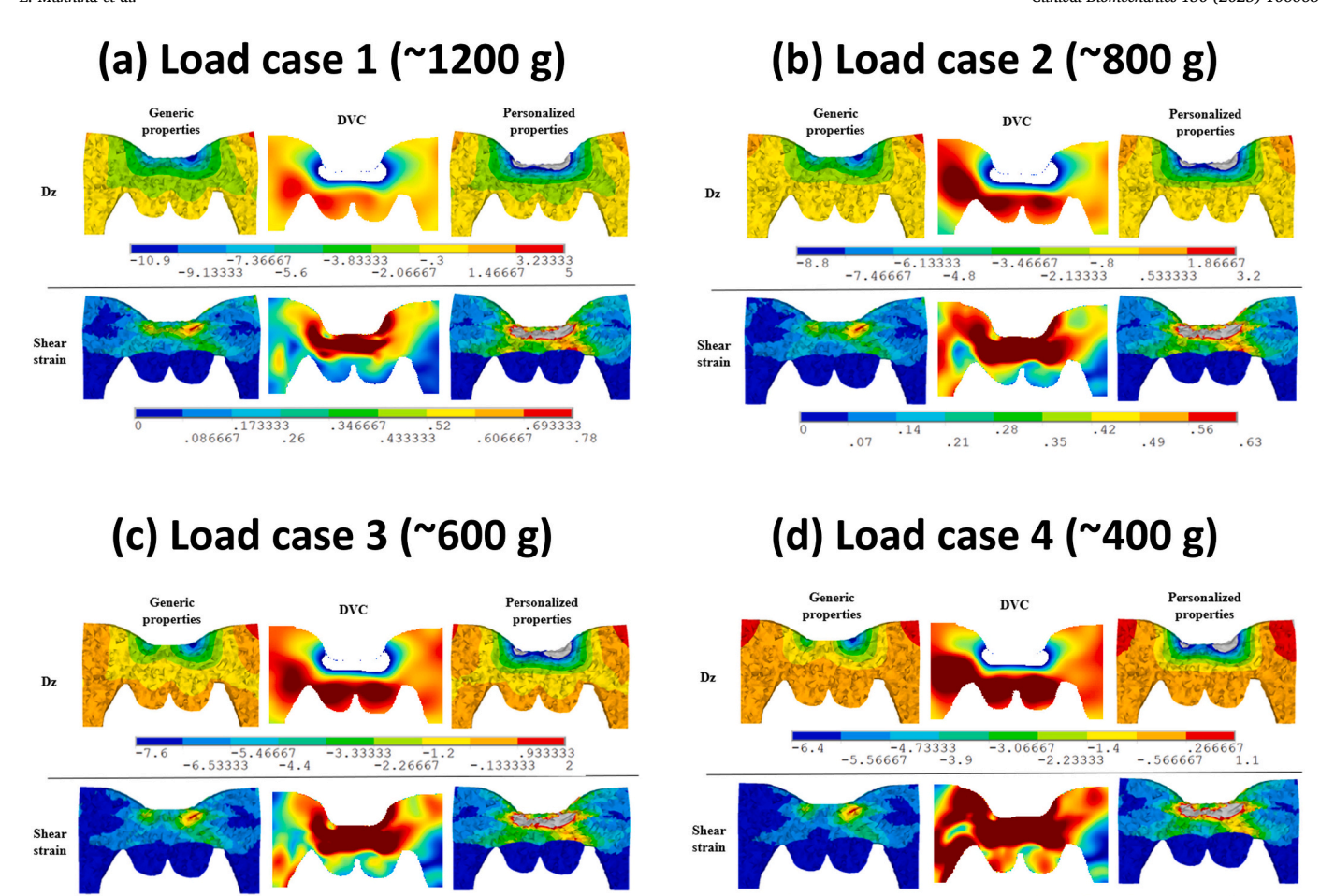


Fig. 7. ANSYS models with generic (left) and personalized (right) material properties compared with DVC (in the center) for evaluating the displacement Dz and double Hencky shear strain, (a) for the Load case 1 (~1200 g) (b) for the load case 2 Load case 2 (~800 g) (c) Load case 3 (~600 g) (d) Load case 4 (~400 g).

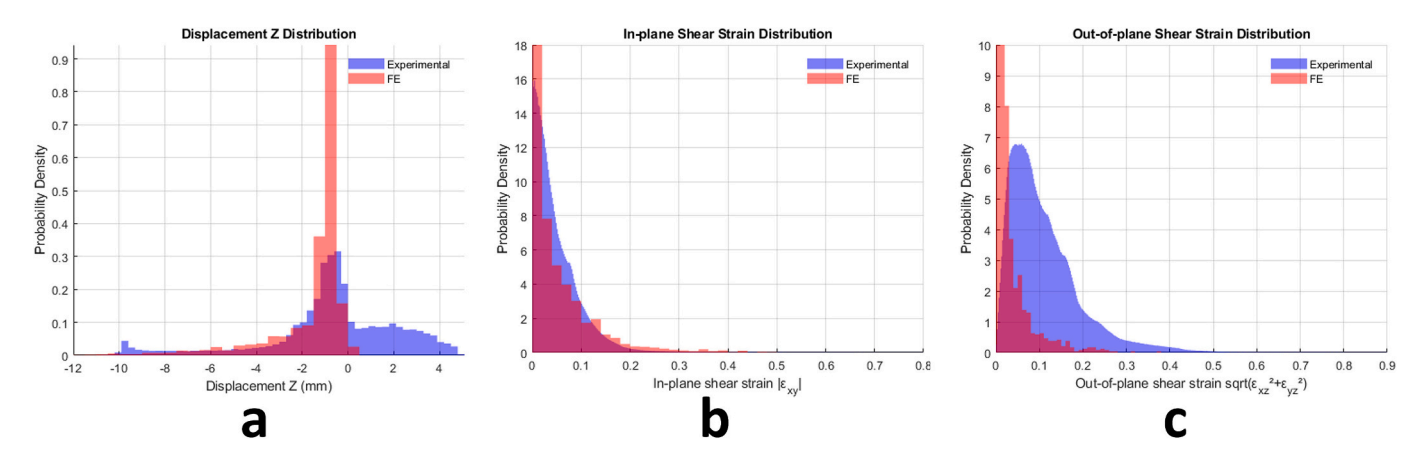


Fig. 8. Comparison of distributions of axial displacement Dz, in-plane shear strains ( $|\epsilon_{xy}|$ ) and out-of-plane shear strains ( $\sqrt{\epsilon_{xz}^2 + \epsilon_{yz}^2}$ ) obtained from DVC measurements (blue) and personalized FE simulations (red) for the highest load case (1.2 kg). Histograms show the probability density functions of each field, illustrating the agreement in displacement and the slight underestimation of shear strains by the FE model, particularly for out-of-plane components.

and mechanical distinctiveness of this region. The sacral soft tissue layer is notably thinner than that over the buttocks, and also well-suited for suction-based in vivo mechanical characterization (VLASTIC), which becomes less reliable in thicker muscle-dominated regions. Establishing experimental evidence that supports FE-predicted relationships between external loading and internal strain in this anatomically challenging area is essential before considering any clinical application.

.122222 .244444 .366667 .488889 .061111 .183333 .305556 .427778 .55

Our findings broadly corroborate previous computational studies indicating that personalization of geometry and boundary conditions significantly improves the predictive capacity of FE models (Luboz et al., 2018; Macron et al., 2020; Segain et al., 2025). However, our work extends this by incorporating subject-specific mechanical properties derived from suction tests. In agreement with sensitivity analyses by (Luboz et al., 2014) we observed that variations

.104444 .208889 .313333 .417778 .052222 .156667 .261111 .365556 .47 in soft tissue stiffness strongly influence predicted strain magnitudes, emphasizing the importance of local mechanical characterization.

To date, quantification of in vivo soft tissue strain in humans remains scarce. Most studies have assessed only global deformations, such as volume or thickness changes between loaded and unloaded configurations (Al-Dirini et al., 2017; Linder-Ganz et al., 2007; Makhsous et al., 2011; Shabshin et al., 2010). However, this approach is limited, especially in light of evidence showing, for example, that rigid body motion of the gluteus maximus compartment occurs during loading (Al-Dirini et al., 2016; Call et al., 2017; Sonenblum et al., 2015). This suggests that thickness changes are not solely due to local compression, challenging strain estimates based only on thickness variation. While 2D strain fields have been estimated from ultrasound sequences (Doridam et al., 2018), these approaches often suffer from poor image quality, yielding variable displacement estimates, and cannot capture complex 3D deformations. In contrast, (Trebbi et al., 2022) were among the first to apply MRIbased Digital Volume Correlation (DVC) to compute full 3D internal strain fields in human soft tissues, including the buttocks and heels, under controlled loading. More recently, (Zappalá et al., 2024) extended this approach specifically to the buttock in semi-recumbent loading conditions. Our study builds directly upon this body of work by comparing displacement and strain fields estimated experimentally using MRI-based DVC to those predicted by an FE model. Like it was previously reported in the literature (Macron et al., 2018; Segain et al., 2025) incorporating personalized calibration of mechanical properties improved agreement with DVC measurements, reducing discrepancies in displacements and shear strains compared to a generic model. Unlike other studies that impose displacement-controlled boundary conditions, our FE model is force-controlled, driven directly by the loads measured with our MR-compatible device, thereby enhancing the biomechanical relevance of the comparison.

In constructing the model, mechanical properties were defined by combining generic literature-derived Yeoh hyperelastic parameters for skin, fat, fascia and muscle (Annaidh et al., 2012; Astruc et al., 2018; Gras et al., 2012; Miller-Young et al., 2002). with subject-specific adjustments of skin and adipose tissue stiffness using VLASTIC suction data, following (Connesson et al., 2023). This allowed a more individualized representation of the mechanical response for the specific volunteer studied. Compared to values commonly reported in the literature, the resulting shear moduli and constitutive parameters are broadly in line for the muscle and fascia. However, the estimated C<sub>10</sub> parameters for the adipose tissue still led to relatively high effective shear moduli. This is a challenge frequently noted in the literature (Affagard et al., 2015a, 2015b; Al-Dirini et al., 2016; Macron et al., 2020). The higher values found in our study likely stem from several factors. First, calibration methods that impose a fixed exponential coefficient in Ogden- or Yeoh-type models can shift the burden of capturing nonlinearity onto the shear modulus, effectively inflating it to compensate for constrained model shapes. In (Al-Dirini et al., 2016) for instance, very different exponential parameters were found for muscle  $(\alpha = 4.6)$  and fat  $(\alpha = 16.2)$  compared to standard assumptions. Moreover, the identification here was primarily based on matching VLASTICderived small-strain moduli and thus constrained to the initial slope of the curve, without data from larger deformations. Recent work by (Fougeron et al., 2024) demonstrated that force-displacement curves alone are insufficient to fully identify hyperelastic parameters, especially when only two states (unloaded and fully loaded) are available. Additional sources of uncertainty come from potential errors in estimating tissue geometry (thickness, curvature) or applied forces during the calibration procedure, which can significantly influence the inferred material properties. Overestimating the applied load, for example, would necessitate stiffer tissue properties to reproduce the observed compression. Despite these limitations, the subject-specific adjustments applied here, based on direct in vivo measurements, still represent a meaningful improvement over purely literature-based values. The reasonable agreement observed in both displacement and shear strain

distributions supports the feasibility of integrating individualized mechanical characterization with advanced imaging-based validation. This is a critical step toward future applications in personalized risk assessment for pressure ulcer prevention, especially in anatomically complex regions like the sacrum where deep tissue injuries remain a major clinical concern.

Importantly, comparing FE predictions to DVC measurements under multiple load levels demonstrated reasonable agreement in displacement fields, with differences under 5 % for three loading cases and about 7 % for the highest load. This is notable given our use of a force-controlled model, which is more biomechanically meaningful than the displacement-controlled conditions often imposed in similar studies. In terms of internal shear strains (key indicators of DTI risk) both FE and DVC showed similar spatial patterns, with peak values consistently located within the adipose layer above the sacral bone rather than directly under the skin, supporting a deep injury mechanism.

This study had some limitations in the definition of the FE model. First and foremost, it is important to acknowledge that this study is based on a single-case evaluation. While the detailed insights gained are valuable for understanding the specific context and intervention examined, the findings have limited transferability and cannot be readily generalized to other populations or settings. Future research involving larger cohorts or multiple case studies would be essential to strengthen the evidence base and explore the broader applicability of these observations.

From a more technical perspective, the segmentation of the geometrical data is performed manually, which could have added inaccuracies in the model. Fasciae are presented as a shell layer with assumed thickness of 0.5 mm, while in reality it is a network of connected tissues. Another limitation is the choice of the subject-specific material properties. The experimental data is limited to the identification of skin and adipose tissues Young moduli, while C20 parameters for both of these tissues are used from the literature. Due to insufficient experimental material data in the literature of sacrum, sacral muscles constitutive laws are based on uniaxial tension data collected on a muscle from the human neck, fascia from experiments on the abdominal wall and adipose tissue from a compression test done on the heel fat pad. Such approximations are necessary given current data availability, but they inevitably affect the fidelity of the model. We recognize, in particular, that using fascia data from the abdominal wall does not accurately capture the properties of the thoracolumbar fascia over the sacrum, which likely has distinct mechanical behaviour. To address this, we have recently performed ex vivo experiments on human thoracolumbar fascia and erector spinae aponeurosis (Creze et al., 2025) and are also developing in vivo identification methods combining indentation, ultrasound imaging, and inverse finite element modelling (Fougeron et al., 2020; Segain et al., 2024). Incorporating these regionspecific data into future models will be critical to improve anatomical fidelity and enhance clinical relevance. Finally, the choice of the Poisson's ratio to enforce near-incompressibility is another parameter that can significantly influence the simulation results, highlighting the need for careful interpretation of quantitative strain predictions. It is worth noting also that while merging nodes at the interfaces between soft tissue layers is a common approach to ensure numerical stability (Al-Dirini et al., 2016; Bucki et al., 2016; Levy et al., 2014; Linder-Ganz et al., 2008b; Macron et al., 2018; Oomens et al., 2013), this does not capture the physiological sliding permitted by fascial structures. Further work is needed to incorporate more realistic interfacial mechanics, which will be essential to enhance the clinical relevance of such models.

Looking forward, we aim to extend this framework by applying it to larger cohorts under more clinically relevant loading scenarios, such as prone positioning, and by incorporating newly acquired region-specific mechanical data. Further improvements will include using higher-resolution MRI to enhance DVC texture, applying tissue-specific registration masks, and employing more precise segmentations to reduce partial volume effects, particularly at interfaces where shear

discrepancies are most pronounced. Additionally, advancing the characterization of large-strain tissue behaviors and refining interfacial contact mechanics to permit realistic sliding will be important for improving shear strain predictions. Incorporating controlled phantom studies with known deformations and conducting sensitivity analyses of model parameters will also help disentangle sources of error attributable to the DVC pipeline versus the FE model itself. These combined steps will be critical to reduce discrepancies, especially in shear, and to move from a research-oriented tool toward a clinically applicable approach for assessing individual DTI risk.

#### 5. Conclusion

In conclusion, this study presented a proof-of-concept for creating subject-specific finite element models of sacral soft tissues under compressive loading, validated against Digital Volume Correlation of MRI data. The models showed close agreement with experimental results for tissue displacement, highlighting their accuracy. However, significant differences in shear strain values point to the need for further refinement. The findings emphasize the importance of personalized material properties in reducing discrepancies between simulations and experimental observations. However, limitations such as manual segmentation, approximations in material properties, and assumptions in model parameters suggest areas for improvement. Future work will focus on enhancing the model by applying it to clinically relevant loading conditions, expanding the cohort size, and including a more representative population of at-risk patients. These efforts will further validate and refine the model, moving closer to potential clinical applications.

#### CRediT authorship contribution statement

Ekaterina Mukhina: Writing – original draft, Software, Methodology, Investigation, Conceptualization. Pierre-Yves Rohan: Writing – review & editing, Visualization, Validation, Supervision, Software, Resources, Methodology, Investigation, Formal analysis, Data curation, Conceptualization. Nathanael Connesson: Writing – review & editing, Visualization, Validation, Supervision, Software, Resources, Methodology, Investigation, Formal analysis, Data curation, Conceptualization. Yohan Payan: Writing – review & editing, Visualization, Validation, Supervision, Software, Resources, Project administration, Methodology, Investigation, Funding acquisition, Formal analysis, Data curation, Conceptualization.

#### Declaration of competing interest

None.

#### Acknowledgement

This project has been funded by the European Union's Horizon 2020 Research and Innovation Programme under Marie Skłodowska-Curie Grant Agreement No. 811965. The IRMaGe MRI facility was partially funded by the French programme "Investissement d'Avenir" of the "Agence Nationale pour la Recherche"; grant "Infrastructure d'avenir en Biologie Sante" - ANR-11-INSB-0006. All authors were fully involved in the study and preparation of the manuscript and that the material within has not been and will not be submitted for publication elsewhere.

#### References

- Affagard, J.S., Feissel, P., Bensamoun, S.F., 2015a. Measurement of the quadriceps muscle displacement and strain fields with ultrasound and digital image correlation (DIC) techniques. Irbm 36, 170–177. https://doi.org/10.1016/j.irbm.2015.02.002.
- Affagard, J.-S., Feissel, P., Bensamoun, S.F., 2015b. Identification of hyperelastic properties of passive thigh muscle under compression with an inverse method from a

- displacement field measurement. J. Biomech. 48, 4081–4086. https://doi.org/10.1016/j.jbiomech.2015.10.007.
- Al-Dirini, R.M.A., Reed, M.P., Hu, J., Thewlis, D., 2016. Development and validation of a high anatomical Fidelity FE model for the buttock and thigh of a seated individual. Ann. Biomed. Eng. 44, 2805–2816. https://doi.org/10.1007/s10439-016-1560-3.
- Al-Dirini, R.M.A., Nisyrios, J., Reed, M.P., Thewlis, D., 2017. Quantifying the in vivo quasi-static response to loading of sub-dermal tissues in the human buttock using magnetic resonance imaging. Clin. Biomech. 50, 70–77. https://doi.org/10.1016/j. clinbiomech.2017.09.017.
- Annaidh, A.N., Bruyère, Karine, Destrade, M., Gilchrist, M.D., Maurini, C., Otténio, M., Saccomandi, G., 2012. Automated estimation of collagen fibre dispersion in the dermis and its contribution to the anisotropic behaviour of skin. Ann. Biomed. Eng. 40, 1666–1678. https://doi.org/10.1007/s10439-012-0542-3.
- Astruc, L., De Meulaere, M., Witz, J.F., Nováček, V., Turquier, F., Hoc, T., Brieu, M., 2018. Characterization of the anisotropic mechanical behavior of human abdominal wall connective tissues. J. Mech. Behav. Biomed. Mater. 82, 45–50. https://doi.org/ 10.1016/j.jmbbm.2018.03.012.
- Barrois, B., Labalette, C., Rousseau, P., Corbin, A., Colin, D., Allaert, F., Saumet, J.I., 2008. A national prevalence study of pressure ulcers in French hospital inpatients. J. Wound Care 17, 373–379. https://doi.org/10.12968/jowc.2008.17.9.30934.
- Bouten, C.V., Oomens, C.W., Baaijens, F.P., Bader, D.L., 2003. The etiology of pressure ulcers: skin deep or muscle bound? Arch. Phys. Med. Rehabil. 84, 616–619. https:// doi.org/10.1053/apmr.2003.50038.
- Briot, N., Chagnon, G., Connesson, N., Payan, Y., 2022. In vivo measurement of breast tissues stiffness using a light aspiration device. Clin. Biomech. 99, 105743. https:// doi.org/10.1016/J.CLINBIOMECH.2022.105743.
- Bucki, M., Luboz, V., Lobos, C., Vuillerme, N., Cannard, F., Diot, B., Payan, Y., 2012.
  Patient-specific finite element model of the buttocks for pressure ulcer prevention linear versus non-linear modelling. Comput. Methods Biomech. Biomed. Engin. 15, 38–40. https://doi.org/10.1080/10255842.2012.713681.
- Bucki, M., Luboz, V., Perrier, A., Champion, E., Diot, B., Vuillerme, N., Payan, Y., 2016. Clinical workflow for personalized foot pressure ulcer prevention. Med. Eng. Phys. 38, 845–853. https://doi.org/10.1016/j.medengphy.2016.04.017.
- Call, E., Hetzel, T., McLean, C., Burton, J.N., Oberg, C., 2017. Off loading wheelchair cushion provides best case reduction in tissue deformation as indicated by MRI. J. Tissue Viability 26, 172–179. https://doi.org/10.1016/j.ity.2017.05.002.
- Ceelen, K.K., Stekelenburg, A., Loerakker, S., Strijkers, G.J., Bader, D.L., Nicolay, K., Baaijens, F.P.T., Oomens, C.W.J., 2008. Compression-induced damage and internal tissue strains are related. J. Biomech. 41, 3399–3404. https://doi.org/10.1016/j. jbiomech.2008.09.016.
- Chimenti, R.L., Flemister, A.S., Ketz, J., Bucklin, M., Buckley, M.R., Richards, M.S., 2016. Ultrasound strain mapping of Achilles tendon compressive strain patterns during dorsiflexion. J. Biomech. 49, 39–44. https://doi.org/10.1016/j. ibiomech.2015.11.008.
- Connesson, N., Briot, N., Rohan, P.Y., Barraud, P.A., Elahi, S.A., Payan, Y., 2023. Bilayer stiffness identification of soft tissues by suction. Exp. Mech. https://doi.org/ 10.1007/s11340-023-00946-x.
- Creze, M., Lagache, A., Duparc, F., Broqué, M., Persohn, S., Slama, C., Vergari, C., Rohan, P.-Y., 2025. Ex vivo mechanical properties of human thoracolumbar fascia and erector spinae aponeurosis under traction loading and shear wave elastography. J. Mech. Behav. Biomed. Mater. 168, 107028. https://doi.org/10.1016/j. jmbbm.2025.107028.
- Demarré, L., Van Lancker, A., Van Hecke, A., Verhaeghe, S., Grypdonck, M., Lemey, J., Annemans, L., Beeckman, D., 2015. The cost of prevention and treatment of pressure ulcers: a systematic review. Int. J. Nurs. Stud. 52, 1754–1774. https://doi.org/ 10.1016/i.inurstu.2015.06.006.
- Doridam, J., Macron, A., Vergari, C., Verney, A., Rohan, P.-Y., Pillet, H., 2018. Feasibility of sub-dermal soft tissue deformation assessment using B-mode ultrasound for pressure ulcer prevention. J. Tissue Viability 27, 238–243. https://doi.org/10.1016/ j.jtv.2018.08.002.
- Elahi, S.A., Connesson, N., Payan, Y., 2018. Disposable system for in-vivo mechanical characterization of soft tissues based on volume measurement. J. Mech. Med. Biol. 18, 1850037. https://doi.org/10.1142/S0219519418500379.
- Elahi, S.A., Connesson, N., Chagnon, G., Payan, Y., 2019. In-vivo soft tissues mechanical characterization: volume-based aspiration method validated on silicones. Exp. Mech. 59, 251–261. https://doi.org/10.1007/s11340-018-00440-9.
- Fougeron, N., Rohan, P.-Y., Haering, D., Rose, J.-L., Bonnet, X., Pillet, H., 2020. Combining freehand ultrasound-based indentation and inverse finite element modeling for the identification of Hyperelastic material properties of thigh soft tissues. J. Biomech. Eng. 142. https://doi.org/10.1115/1.4046444.
- tissues. J. Biomech. Eng. 142. https://doi.org/10.1115/1.4046444.

  Fougeron, N., Connesson, N., Chagnon, G., Alonso, T., Pasquinet, L., Bahuon, M., Guillin, E., Perrier, A., Payan, Y., 2022. New pressure ulcers dressings to alleviate human soft tissues: a finite element study. J. Tissue Viability. https://doi.org/10.1016/j.jtv.2022.05.007.
- Fougeron, N., Oddes, Z., Ashkenazi, A., Solav, D., 2024. Identification of constitutive materials of bi-layer soft tissues from multimodal indentations. J. Mech. Behav. Biomed. Mater. 155, 106572. https://doi.org/10.1016/j.jmbbm.2024.106572.
- Gras, L.L., Mitton, D., Viot, P., Laporte, S., 2012. Hyper-elastic properties of the human sternocleidomastoideus muscle in tension. J. Mech. Behav. Biomed. Mater. 15, 131–140. https://doi.org/10.1016/j.jmbbm.2012.06.013.
- Kappert, K.D.R., Connesson, N., Elahi, S.A., Boonstra, S., Balm, A.J.M., van der Heijden, F., Payan, Y., 2021. In-vivo tongue stiffness measured by aspiration: resting vs general anesthesia. J. Biomech. 114, 110147. https://doi.org/10.1016/j. jbiomech.2020.110147.

- Klein, S., Staring, M., Murphy, K., Viergever, M.A., Pluim, J.P.W., 2010. Elastix: a toolbox for intensity-based medical image registration. IEEE Trans. Med. Imaging 29, 196–205. https://doi.org/10.1109/TMI.2009.2035616.
- Lahmann, N.A., Halfens, R.J.G., Dassen, T., 2005. Prevalence of pressure ulcers in Germany. J. Clin. Nurs. 14, 165–172. https://doi.org/10.1111/j.1365-2702.2004.01037.x.
- Levy, A., Kopplin, K., Gefen, A., 2013. Simulations of skin and subcutaneous tissue loading in the buttocks while regaining weight-bearing after a push-up in wheelchair users. J. Mech. Behav. Biomed. Mater. 28, 436–447. https://doi.org/10.1016/j. imbbm.2013.04.015.
- Levy, A., Kopplin, K., Gefen, A., 2014. An air-cell-based cushion for pressure ulcer protection remarkably reduces tissue stresses in the seated buttocks with respect to foams: finite element studies. J. Tissue Viability 23, 13–23. https://doi.org/ 10.1016/i.jty.2013.12.005.
- Levy, A., Schwartz, D., Gefen, A., 2017. The contribution of a directional preference of stiffness to the efficacy of prophylactic sacral dressings in protecting healthy and diabetic tissues from pressure injury: computational modelling studies. Int. Wound J. 14, 1370–1377. https://doi.org/10.1111/iwj.12821.
- Linder-Ganz, E., Shabshin, N., Itzchak, Y., Yizhar, Z., Siev-Ner, I., Gefen, A., 2008. Strains and stresses in sub-dermal tissues of the buttocks are greater in paraplegics than in healthy during sitting. J. Biomech. 41, 567–580. https://doi.org/10.1016/j. ibiomech.2007.10.011.
- Linder-Ganz, E., Shabshin, N., Itzchak, Y., Gefen, A., 2007. Assessment of mechanical conditions in sub-dermal tissues during sitting: a combined experimental-MRI and finite element approach. J. Biomech. 40, 1443–1454. https://doi.org/10.1016/j. ibiomech. 2006.06.020
- Linder-Ganz, E., Yarnitzky, G., Yizhar, Z., Siev-Ner, I., Gefen, A., 2009. Real-time finite element monitoring of sub-dermal tissue stresses in individuals with spinal cord injury: toward prevention of pressure ulcers. Ann. Biomed. Eng. 37, 387–400. https://doi.org/10.1007/s10439-008-9607-8.
- Loerakker, S., Bader, D.L., Baaijens, F.P.T., Oomens, C.W.J., 2013. Which factors influence the ability of a computational model to predict the in vivo deformation behaviour of skeletal muscle? Comput. Methods Biomech. Biomed. Engin. 16, 338–345. https://doi.org/10.1080/10255842.2011.621423.
- Luboz, V., Petrizelli, M., Bucki, M., Diot, B., Vuillerme, N., Payan, Y., 2014. Biomechanical modeling to prevent ischial pressure ulcers. J. Biomech. 47, 2231–2236. https://doi.org/10.1016/j.jbiomech.2014.05.004.
- Luboz, V., Bailet, M., Boichon Grivot, C., Rochette, M., Diot, B., Bucki, M., Payan, Y., 2018. Personalized modeling for real-time pressure ulcer prevention in sitting posture. J. Tissue Viability 27, 54–58. https://doi.org/10.1016/j.jtv.2017.06.002.
- Machado, I., Toews, M., George, E., Unadkat, P., Essayed, W., Luo, J., Teodoro, P., Carvalho, H., Martins, J., Golland, P., Pieper, S., Frisken, S., Golby, A., William Wells, I.I.I., Ou, Y., 2019. Deformable MRI-ultrasound registration using correlation-based attribute matching for brain shift correction: accuracy and generality in multisite data. NeuroImage 202, 116094. https://doi.org/10.1016/j.neuroimage.2019.116094.
- Macron, A., Pillet, H., Doridam, J., Verney, A., Rohan, P.-Y., 2018. Development and evaluation of a new methodology for the fast generation of patient-specific finite element models of the buttock for sitting-acquired deep tissue injury prevention. J. Biomech. 79, 173–180. https://doi.org/10.1016/j.jbiomech.2018.08.001.
- Macron, A., Pillet, H., Doridam, J., Rivals, I., Sadeghinia, M.J., Verney, A., Rohan, P.-Y., 2020. Is a simplified finite element model of the gluteus region able to capture the mechanical response of the internal soft tissues under compression? Clin. Biomech. 71, 92–100. https://doi.org/10.1016/j.clinbiomech.2019.10.005.
- Makhsous, M., Lin, F., Cichowski, A., Cheng, I., Fasanati, C., Grant, T., Hendrix, R.W., 2011. Use of MRI images to measure tissue thickness over the ischial tuberosity at different hip flexion. Clin. Anat. 24, 638–645. https://doi.org/10.1002/ca.21119.
- McAuliffe, P.B., Winter, E.E., Talwar, A.A., Desai, A.A., Broach, R.B., Fischer, J.P., 2023. Pressure ulcer trends in the United States: a cross-sectional assessment from 2008-2019. Am. Surg. 89, 5609–5618. https://doi.org/10.1177/00031348231158691.
- Miller-Young, J.E., Duncan, N.A., Baroud, G., 2002. Material properties of the human calcaneal fat pad in compression: experiment and theory. J. Biomech. 35, 1523–1531. https://doi.org/10.1016/S0021-9290(02)00090-8.
- Mimura, M., Ohura, T., Takahashi, M., Kajiwara, R., Ohura, N., 2009. Mechanism leading to the development of pressure ulcers based on shear force and pressures during a bed operation: influence of body types, body positions, and knee positions. Wound Repair Regen. 17, 789–796. https://doi.org/10.1111/j.1524-475X.2009.00540.x.
- Moerman, K.M., van Vijven, M., Solis, L.R., van Haaften, E.E., Loenen, A.C.Y., Mushahwar, V.K., Oomens, C.W.J., 2017. On the importance of 3D, geometrically accurate, and subject-specific finite element analysis for evaluation of in-vivo soft tissue loads. Comput. Methods Biomech. Biomed. Engin. 20, 483–491. https://doi. org/10.1080/10255842.2016.1250259.

- Mott, P.H., Dorgan, J.R., Roland, C.M., 2008. The bulk modulus and Poisson's ratio of "incompressible" materials. J. Sound Vib. 312, 572–575. https://doi.org/10.1016/j.isv.2008.01.026
- Mukhina, E., Trebbi, A., Rohan, P.-Y., Connesson, N., Payan, Y., 2022. In vivo quantification of 3D displacement in sacral soft tissues under compression: relevance of 2D US-based measurements for pressure ulcer risk assessment. J. Tissue Viability 31, 593–600. https://doi.org/10.1016/j.jtv.2022.09.007.
- Oomens, C.W.J., 2013. A multilevel finite element approach to study pressure ulcer Aetiology. In: Multiscale Computer Modeling in Biomechanics and Biomedical Engineering, Studies in Mechanobiology, Tissue Engineering and Biomaterials. Springer, Berlin, Heidelberg, pp. 289–298. https://doi.org/10.1007/8415\_2012\_150
- Oomens, C.W.J., Zenhorst, W., Broek, M., Hemmes, B., Poeze, M., Brink, P.R.G., Bader, D.L., 2013. A numerical study to analyse the risk for pressure ulcer development on a spine board. Clin. Biomech. 28, 736–742. https://doi.org/ 10.1016/j.clinbiomech.2013.07.005.
- Oomens, C.W.J., Bader, D.L., Loerakker, S., Baaijens, F., 2015. Pressure induced deep tissue injury explained. Ann. Biomed. Eng. 43, 297–305. https://doi.org/10.1007/ s10439-014-1202-6.
- Padula, W.V., Delarmente, B.A., 2019. The national cost of hospital-acquired pressure injuries in the United States. Int. Wound J. 16, 634–640. https://doi.org/10.1111/ iwi.13071.
- Rohan, P.-Y., Fougeron, N., Keenan, B., Pillet, H., Laporte, S., Osipov, N., Ryckelynck, D., 2023. Chapter 20 - real-time numerical prediction of strain localization using dictionary-based ROM-nets for sitting-acquired deep tissue injury prevention. In: Chinesta, F., Cueto, E., Payan, Y., Ohayon, J. (Eds.), Reduced Order Models for the Biomechanics of Living Organs, Biomechanics of Living Organs. Academic Press, pp. 385–402. https://doi.org/10.1016/B978-0-32-389967-3.00027-5.
- Schreml, S., Berneburg, M., 2017. The global burden of diabetic wounds. Br. J. Dermatol. 176, 845–846. https://doi.org/10.1111/bjd.15254.
- Segain, A., Sciume, G., Pillet, H., Rohan, P.-Y., 2024. In vivo mechanical response of thigh soft tissues under compression: a two-layer model allows an improved representation of the local tissue kinematics. J. Mech. Behav. Biomed. Mater. 156, 106584. https:// doi.org/10.1016/j.jmbbm.2024.106584.
- Segain, A., Pillet, H., Zappalá, S., Sciume, G., Rohan, P.-Y., 2025. Corroboration in vivo mechanical strain distribution in soft tissues for pressure ulcer prevention: a comparative analysis between a simplified finite element analysis and experimental strain fields. J. Mech. Behav. Biomed. Mater. 168, 107017. https://doi.org/10.1016/ j.jmbbm.2025.107017.
- Shabshin, N., Zoizner, G., Herman, A., Ougortsin, V., Gefen, A., 2010. Use of weight-bearing MRI for evaluating wheelchair cushions based on internal soft-tissue deformations under ischial tuberosities. J. Rehabil. Res. Dev. 47, 31. https://doi.org/10.1682/JRRD.2009.07.0105.
- Sonenblum, S.E., Sprigle, S.H., Cathcart, J.M., Winder, R.J., 2015. 3D anatomy and deformation of the seated buttocks. J. Tissue Viability 24, 51–61. https://doi.org/ 10.1016/j.itv.2015.03.003.
- Sopher, R., Nixon, J., Gorecki, C., Gefen, A., 2010. Exposure to internal muscle tissue loads under the ischial tuberosities during sitting is elevated at abnormally high or low body mass indices. J. Biomech. 43, 280–286. https://doi.org/10.1016/j. ibiomech. 2009.08.021
- Stekelenburg, A., Strijkers, G.J., Parusel, H., Bader, D.L., Nicolay, K., Oomens, C.W., 2007. Role of ischemia and deformation in the onset of compression-induced deep tissue injury: MRI-based studies in a rat model. J. Appl. Physiol. 102, 2002–2011. https://doi.org/10.1152/japplphysiol.01115.2006.
- Traa, W.A., van Turnhout, M.C., Nelissen, J.L., Strijkers, G.J., Bader, D.L., Oomens, C.W. J., 2019. There is an individual tolerance to mechanical loading in compression induced deep tissue injury. Clin. Biomech. 63, 153–160. https://doi.org/10.1016/j.clinbiomech.2019.02.015.
- Trebbi, A., Mukhina, E., Rohan, P.-Y., Connesson, N., Bailet, M., Perrier, A., Payan, Y., 2022. Medical engineering and physics MR-based quantitative measurement of human soft tissue internal strains for pressure ulcer prevention. Med. Eng. Phys. 108, 1–10. https://doi.org/10.1016/j.medengphy.2022.103888.
- Vanderwee, K., Clark, M., Dealey, C., Gunningberg, L., Defloor, T., 2007. Pressure ulcer prevalence in Europe: a pilot study. J. Eval. Clin. Pract. 13, 227–235. https://doi. org/10.1111/j.1365-2753.2006.00684.x.
- Zappalá, S., Keenan, B.E., Marshall, D., Wu, J., Evans, S.L., Al-Dirini, R.M.A., 2024. In vivo strain measurements in the human buttock during sitting using MR-based digital volume correlation. J. Biomech. 163, 111913. https://doi.org/10.1016/j. ibiomech.2023.111913.
- Zhu, Haijiang, Zhou, Shifeng, Yang, Ping, Longbiao He, J.Z., 2015. An efficient optimal method for a 2D strain estimation of ultrasound tissue-mimicking material phantom. Polym. Eng. Sci. 55, 2751–2760.